*remote sensing*

MDPI

*Article*

# Integrated Remote Sensing Investigation of Suspected Landslides: A Case Study of the Genie Slope on the Tibetan Plateau, China

**Wenlong Yu [1], Weile Li [1,*], Zhanglei Wu [2], Huiyan Lu [1], Zhengxuan Xu [3], Dong Wang [3], Xiujun Dong [1] and Pengfei Li [4]**

[1] State Key Laboratory of Geohazard Prevention and Geoenvironment Protection, Chengdu University of Technology, Chengdu 610059, China; wenlongyu@stu.cdut.edu.cn (W.Y.); 2017050002@stu.cdut.edu.cn (H.L.); dongxiujun@cdut.edu.cn (X.D.)
[2] Chengdu Engineering Co., Ltd., Power Construction Corporation, Chengdu 610072, China; 2000016@chidi.com.cn
[3] China Railway Eryuan Engineering Group Co., Ltd., Chengdu 610031, China; xuzhengx@ey.crec.cn (Z.X.); wangdong13@ey.crec.cn (D.W.)
[4] Guiyang Engineering Corporation Limited of Power China, Guiyang, 550081, China; lipengfei_gyy@powerchina.cn
* Correspondence: liweile08@mail.cdut.edu.cn

**Abstract:** The current deformation and stable state of slopes with historical shatter signs is a concern for engineering construction. Suspected landslide scarps were discovered at the rear edge of the Genie slope on the Tibetan Plateau during a field investigation. To qualitatively determine the current status of the surface deformation of this slope, this study used high-resolution optical remote sensing, airborne light detection and ranging (LiDAR), and interferometric synthetic aperture radar (InSAR) technologies for comprehensive analysis. The interpretation of high-resolution optical and airborne LiDAR data revealed that the rear edge of the slope exhibits three levels of scarps. However, no deformation was detected with differential InSAR (D-InSAR) analysis of ALOS-1 radar images from 2007 to 2008 or with Stacking-InSAR and small baseline subset InSAR (SBAS-InSAR) processing of Sentinel-1A radar images from 2017 to 2020. This study verified the credibility of the InSAR results using the standard deviation of the phase residuals, as well as in-borehole displacement monitoring data. A conceptual model of the slope was developed by combining field investigation, borehole coring, and horizontal exploratory tunnel data, and the results indicated that the slope is composed of steep anti-dip layered dolomite limestone and that the scarps at the trailing edges of the slope were caused by historical shallow toppling. Unlike previous remote sensing studies of deformed landslides, this paper argues that remote sensing results with reliable accuracy are also applicable to the study of undeformed slopes and can help make preliminary judgments about the stability of unexplored slopes. The study demonstrates that the long-term consistency of InSAR results in integrated remote sensing can serve as an indicator for assessing slope stability.

**Keywords:** suspected landslide; slope deformation; stability; optical remote sensing; LiDAR; stacking-InSAR; SBAS-InSAR

check for updates

**Citation:** Yu, W.; Li, W.; Wu, Z.; Lu, H.; Xu, Z.; Wang, D.; Dong, X.; Li, P. Integrated Remote Sensing Investigation of Suspected Landslides: A Case Study of the Genie Slope on the Tibetan Plateau, China. *Remote Sens.* **2024**, *16*, 2412. https://doi.org/10.3390/rs16132412

Academic Editor: Michele Saroli

Received: 23 May 2024
Revised: 24 June 2024
Accepted: 27 June 2024
Published: 1 July 2024

**Copyright:** © 2024 by the authors. Licensee MDPI, Basel, Switzerland. This article is an open access article distributed under the terms and conditions of the Creative Commons Attribution (CC BY) license (https://creativecommons.org/licenses/by/4.0/).

## 1. Introduction

The Tibetan Plateau, as the third pole of the Earth, is a zone of rapid topographic change characterized by plate collision and active tectonics. The eastern part of the plateau, in particular, is marked by complex topography, active plate tectonics, and extremely high seismic intensity. The complex and varied geological conditions indicate the development of geological hazards [1–7]. Early studies showed that most of the famous large-scale landslide disasters on the Qinghai–Tibet Plateau occurred in the area of deeply incised valleys [8–12]. The Sichuan–Tibet transport corridor improves the connectivity of the

country's regional economy and promotes the development of public education, culture, healthcare, and social security. The rationality of the route not only affects the safe operation of the line at a later stage but also influences the planning of high-intensity maintenance programs. Often, the best-designed routes are located in the lower sections of the slopes along the river. Therefore, the stability of the slopes poses a considerable challenge to the routing and design of the Sichuan–Tibet transport corridor.

With the rapid development of various remote sensing technologies and the significant increase in successful applications in geological disaster investigations, integrated remote sensing has become a common method for identifying and monitoring geological disasters. This approach analyzes the displacement and deformation processes of geological disasters in conjunction with other geological measurements, establishes detailed geological models, and further assesses the risk of geological disasters [13,14]. Common remote sensing techniques include high-precision optical remote sensing, light detection and ranging (LiDAR) remote sensing, and interferometric synthetic aperture radar (InSAR), each offering unique advantages in different aspects [15,16]. High-resolution optical satellite remote sensing data have the advantage of originating from multiple sources and being acquired over multiple temporal scales with low acquisition costs and wide coverage; hence, optical data are widely used in railway route selection surveys and geohazard investigations for existing lines [17,18]. In contrast, LiDAR data have a higher resolution than optical data and provide more realistic surface information through the processing of point cloud data, making it possible to achieve more detailed identification and interpretation of geohazard bodies [19–21]. Consequently, LiDAR technology offers irreplaceable advantages in railway surveys [22–25]. As another alternative, InSAR technology plays an important role in the rapid identification and monitoring of surface deformation along railway lines by virtue of its ability to acquire measurements at all times of day and under all weather conditions, and it can achieve deformation monitoring accuracy up to the millimeter scale [26–32]. Although InSAR technology has many limitations, it has developed from the initial D-InSAR (differential InSAR) technique to subsequent time series analysis technologies, such as small baseline subset InSAR (SBAS-InSAR), persistent scatterer InSAR (PS-InSAR), and stacking-InSAR; this development has been accomplished by continuously diminishing the influence of factors such as spatiotemporal decoherence, atmospheric delays, and noise. By distinguishing and eliminating phases that are not related to the deformation phase, more reliable deformation estimates can be obtained [33–39]. Just as InSAR technology has various drawbacks, individual remote sensing techniques have their own shortcomings; however, integrated remote sensing can compensate for these disadvantages and provide a more comprehensive assessment of geological hazards. In previous disaster studies, integrated remote sensing techniques were mostly used for slopes that were undergoing slow deformation, while less research has been conducted on slopes with only morphological features but no deformation [40]. In contrast, this study was conducted for the latter type of slope. The visual identification of these slopes suggests a landslide-like morphology, yet the InSAR technique indicates no deformation. By leveraging InSAR technology to retrieve historical deformation data on the slopes, the non-deformation results can be inferred to denote current stability. Additionally, employing optical, LiDAR, and other visual identification technologies to discern slope structural characteristics and further deduce formation mechanisms significantly reduces the cost and time associated with physical exploration during route selection phases.

In this paper, three remote sensing techniques, namely, optical remote sensing, airborne LiDAR, and InSAR, were integrated to detect, identify, and interpret the deformation of the slope of the Genie Tunnel, which is located on the Batang to Jinsha River section of the Sichuan–Tibet transportation corridor. High-resolution optical satellite images, airborne LiDAR-derived data (DEM and hillshade), and Advanced Land Observing Satellite (ALOS)-1 and Sentinel-1A satellite data were collected. The results of the analyses of these three datasets, as well as the data from the field survey, were combined to assess the stability of the Genie slope and to explain the mechanisms of its formation. This study enhances the

assessment of suspected landslide terrain along the Sichuan–Tibet transport corridor. It demonstrates the feasibility of this approach and underscores the significance of InSAR long-term consistency in integrated remote sensing. Furthermore, it provides a valuable reference for subsequent engineering pre-investigations of slopes along similar transport corridors.

## 2. Slope Conditions

The Genie slope is located approximately 4 km south of Huolong Village, Gaiyu Town, Baiyu County, Ganzi Prefecture, Sichuan Province. The slope is located on the left bank of the Jiangqu River within a typical alpine canyon area, with the NW–SE-trending Jinsha River east boundary fault passing through the foot of the slope (Figure 1a,b). The elevation of the top of the slope is 4535 m, and the elevation of the Jiangqu River, which flows through the foot of the front edge, is 3140 m. The relative height difference reaches 1395 m, and the average slope is 67%. The overall horizontal length of the slope is approximately 2 km, and the width is approximately 1.8 km (Figure 1c). The structure is an inverted, steeply inclined layered rock slope, on which the overlying soil layer is composed of Quaternary residues and slope deposits. The Lower Devonian Ganxi Formation ($D_1g$) strata are exposed in the upper part of the slope, and the Upper Silurian Yongren Formation ($S_3y$) strata are exposed in the middle and lower parts. The lithology of both groups of exposed strata is mainly dolomite limestone.

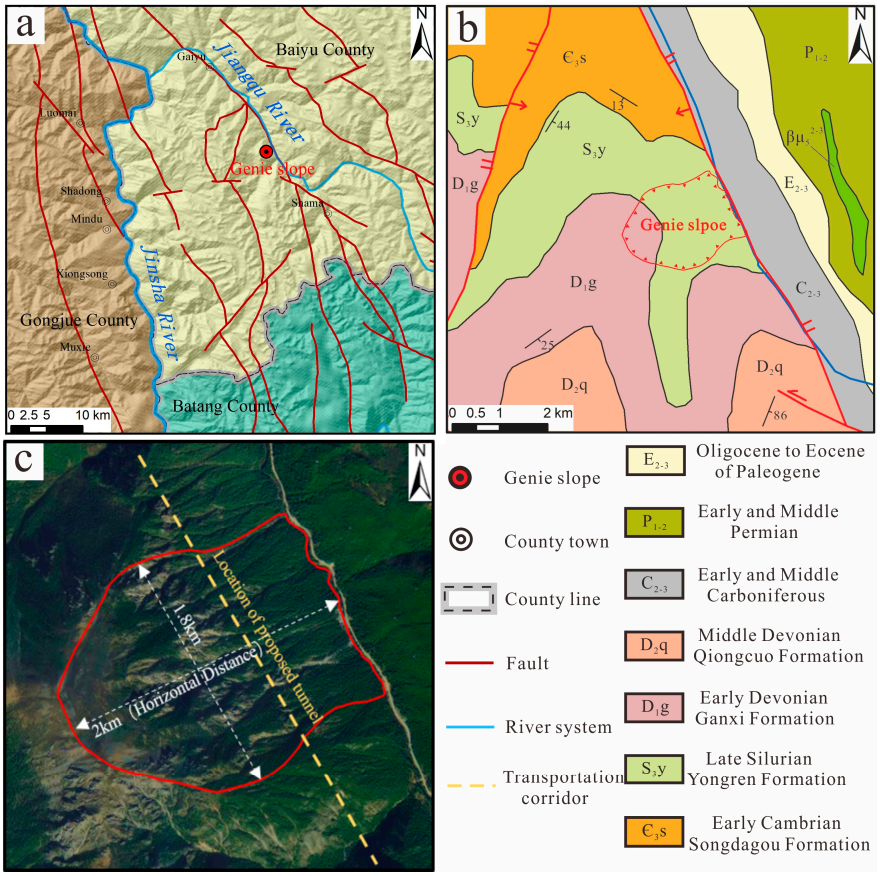



**Figure 1.** Geographical and geological conditions of the study area. (**a**) Location of the study area; (**b**) geological overview of the study area; (**c**) remote sensing image of the Genie slope.

To cross the slope of Genie Mountain, the Sichuan–Tibet transportation corridor was designed to adopt a tunneling method. The proposed route is located in the middle and lower parts of the slope. Therefore, whether a slope is experiencing deformation constitutes a vital component in determining the feasibility of the design scheme.

## 3. Data and Methodology

### 3.1. Datasets

#### 3.1.1. Optical Satellite Imagery and Airborne LiDAR Data

For this research, true-color satellite optical image data with a resolution of 0.5 m taken by the WorldView-2 satellite in March 2015 were collected. These satellite optical image data are of good quality, and the resolution reaches the submeter level; there is no cloud cover, and there are no large backlit areas in the image footprint. The image data perfectly cover the research area and clearly show the morphological and deformation characteristics of the slope. The optical images were registered and geometrically rectified using multi-period satellite imagery and high-precision DEM data from airborne LiDAR. Accordingly, the data met the basic requirements for visual interpretation.

In addition, 3D laser point cloud data acquired by SKYEYE SE-J1200B airborne LiDAR were collected. When the point cloud density is greater than 50 points/$m^3$, the difference between the point cloud air strips is greater than 10 cm. The TerraScan and TerraModeler modules of the Terrasolid software were used to automatically classify the raw point cloud data, and the point clouds were classified into ground, vegetation, and noise point types. Then, the ground point cloud data were manually edited and corrected to obtain ground point cloud data, and a high-accuracy real surface digital elevation model (DEM) and hillshade model were generated in ArcGIS software based on the ground point cloud data.

#### 3.1.2. SAR Data

In this study, ascending L-band spaceborne SAR image data captured by the phased array type L-band synthetic aperture radar (PALSAR) sensor on board the ALOS-1 satellite launched by the Japan Aerospace Development and Research Agency (JAXA) were used for D-InSAR analysis. The time span of the collected ALOS-1 data is from January 2007 to December 2008. However, although the satellite has a revisit period of 46 days, only 9 scenes of ascending data were collected within this time span due to the influence of the data source. Nevertheless, compared with other SAR image data, the wavelength of 23.6 cm enables the ALOS-1 data to maintain a certain degree of coherence over a longer time interval, so the 9 collected data scenes meet the processing requirements of D-InSAR technology.

Furthermore, 108 scenes of ascending SAR image data acquired by the Sentinel-1A Earth-observing satellite launched by the European Space Agency (ESA) were acquired over the period from March 2017 to November 2020. The image interval between two adjacent scenes is 12 days, and the image time series are continuous, which is suitable for time series InSAR analysis. The basic parameters of these two spaceborne SAR image datasets are summarized in Table 1, and their spatial extents are depicted in Figure 2.

**Table 1.** Parameters of the SAR image data used in this study.

| Parameters | SAR Sensors | |
|---|---|---|
| | **ALOS PALSAR-1** | **Sentinel-1A** |
| Polarization mode | HH | VV |
| Spatial resolution (m) | 10 × 10 | 5 × 20 |
| Incidence angle (°) | 34.3 | 39.5 |
| Orbit | Ascending | Ascending |
| Band (Radar wavelength/cm) | L (23.6) | C (5.6) |
| Period | July 2007–December 2008 | March 2017–November 2020 |
| Number of images | 9 | 108 |

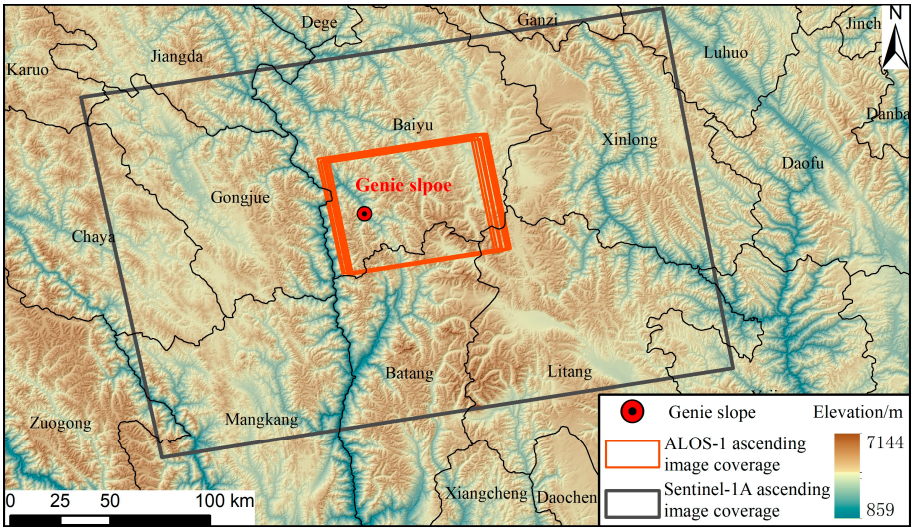



**Figure 2.** Coverage of the SAR images used in this study.

### *3.2. Methodology*

The slope morphological characteristics were analyzed using optical satellite images and airborne LiDAR DEM and hillshade data, while the deformation of the slope was monitored using three different InSAR techniques (D-InSAR, Stacking-InSAR and SBAS-InSAR). Based on the above studies, field investigations were conducted to verify the results of the remote sensing analysis. Subsequently, all the conclusions were summarized to analyze the current status of slope deformation and to establish a geological model of slopes to analyze the slope evolution process. The technical flowchart adopted in this study is shown in Figure 3. In the diagram, the red boxes represent the remote sensing technology module; the yellow boxes denote the data processing methods and results module; the blue boxes signify the integrated remote sensing analysis module; the green boxes correspond to the various field investigations module; and the purple box indicates the slope mechanism analysis module. The remote sensing analysis was divided into two main modules, namely, visual interpretation of slopes and deformation detection, as described below.

#### 3.2.1. Optical Remote Sensing and Airborne LiDAR Interpretation

Manual visual interpretation was employed for both optical remote sensing and LiDAR 3D digital models. When interpreting the optical remote sensing data, it is crucial to identify morphological features and any signs of deformation on the Genie slope. Elements of interpretation include color, feature size, texture, shape, and shading conditions of the image. The study interprets the data based on overall features, such as slope shape, boundary conditions, and vegetation cover. Local features focus on negative topographic conditions at the back edge of the slope, development of hazardous rocks in the center, and deformation characteristics of the river channel at the front edge. Signs of deformation include local cracks or secondary failures at the foot of the slope. High-resolution DEM and hillshade data were utilized to analyze slope characteristics in densely vegetated areas. By removing vegetation, more realistic hillshade data can be obtained, allowing detailed examination of the topography in the central part of the slope and identification of accumulation characteristics on the leading edge. Additionally, this method helps measure the structural surface of the slope, further defining the basic yield of the slope rock mass and providing support for subsequent analyses of the slope mechanism.

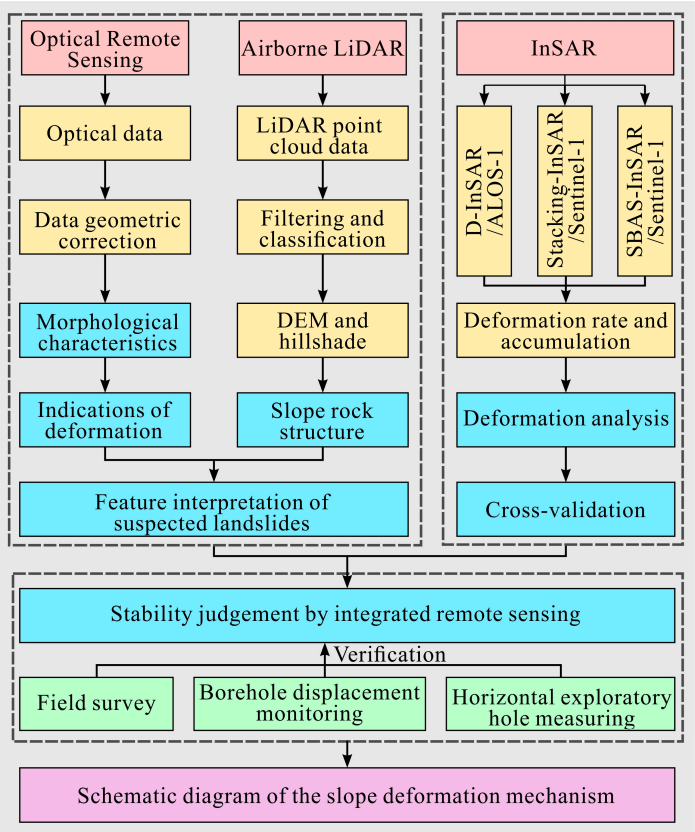



**Figure 3.** Technical workflow adopted in this study.

#### 3.2.2. InSAR Deformation Monitoring

Based on GAMMA SAR and interferometric processing software, D-InSAR, Stacking-InSAR, and SBAS-InSAR technologies were applied to carry out deformation monitoring research. D-InSAR was applied to every two adjacent scenes of ALOS-1 time series data to obtain filtered differential interferograms, and the geocoded unwrapped differential interferograms were used to determine the deformation of the Genie slope according to the phase change characteristics. In addition, time series analyses were conducted using Stacking-InSAR and SBAS-InSAR for the Sentinel-1A data. Stacking-InSAR performs a weighted superposition of a series of unwrapped differential interferograms to obtain the average deformation phase over a certain period, where the accuracy of the final deformation increases with the time span and amount of superimposed data [41,42]. A maximum temporal baseline of 60 days was set for this study, and a total of 318 interferometric image pairs were generated. A window size of 3 pixels is set for coherence evaluation during differential interferometry. Subsequently, a window size of 32 pixels is employed for filtering to enhance coherence. The Delaunay triangulation method in minimum cost flow is then utilized to recover the true phase. All the unwrapped interference image pairs were stacked year by year to obtain interferometric stacking maps for 2017, 2018, 2019, and 2020, and the deformation of the Genie slope was evaluated through the four interferometric stacking maps. The SBAS-InSAR was also employed to further obtain the average deformation rate and historical displacement of the Genie slope over a period of three and a half years and to evaluate the deformation of the Genie slope by statistically analyzing the deformation rate and displacement of typical deformation points in the slope. During the SBAS-InSAR processing, points with coherence greater than 0.4 are selected to contribute to the deformation solution. Subsequently, points with a standard deviation of phase residuals less than 2.5 radians are retained for slope deformation analysis.

By employing two radar satellite datasets and three InSAR techniques, this study comprehensively analyzed the deformation of the slope. The deformation data obtained from

various datasets and InSAR methods are integrated into a unified coordinate system. The results undergo cross-verification to compare deformation trends and features across each InSAR dataset. Additionally, optical and airborne LiDAR data are overlaid to analyze slope surface and terrain features corresponding to different deformation datasets. Furthermore, field surveys provided additional support for confirming the deformation characteristics observed through remote sensing analysis.

## 4. Results

### *4.1. Optical Remote Sensing and Airborne LiDAR Interpretation Results*

Based on the analysis of optical and LiDAR images, the Genie slope can be categorized into three distinct zones based on its geological and deformation characteristics (Figure 4a,b).

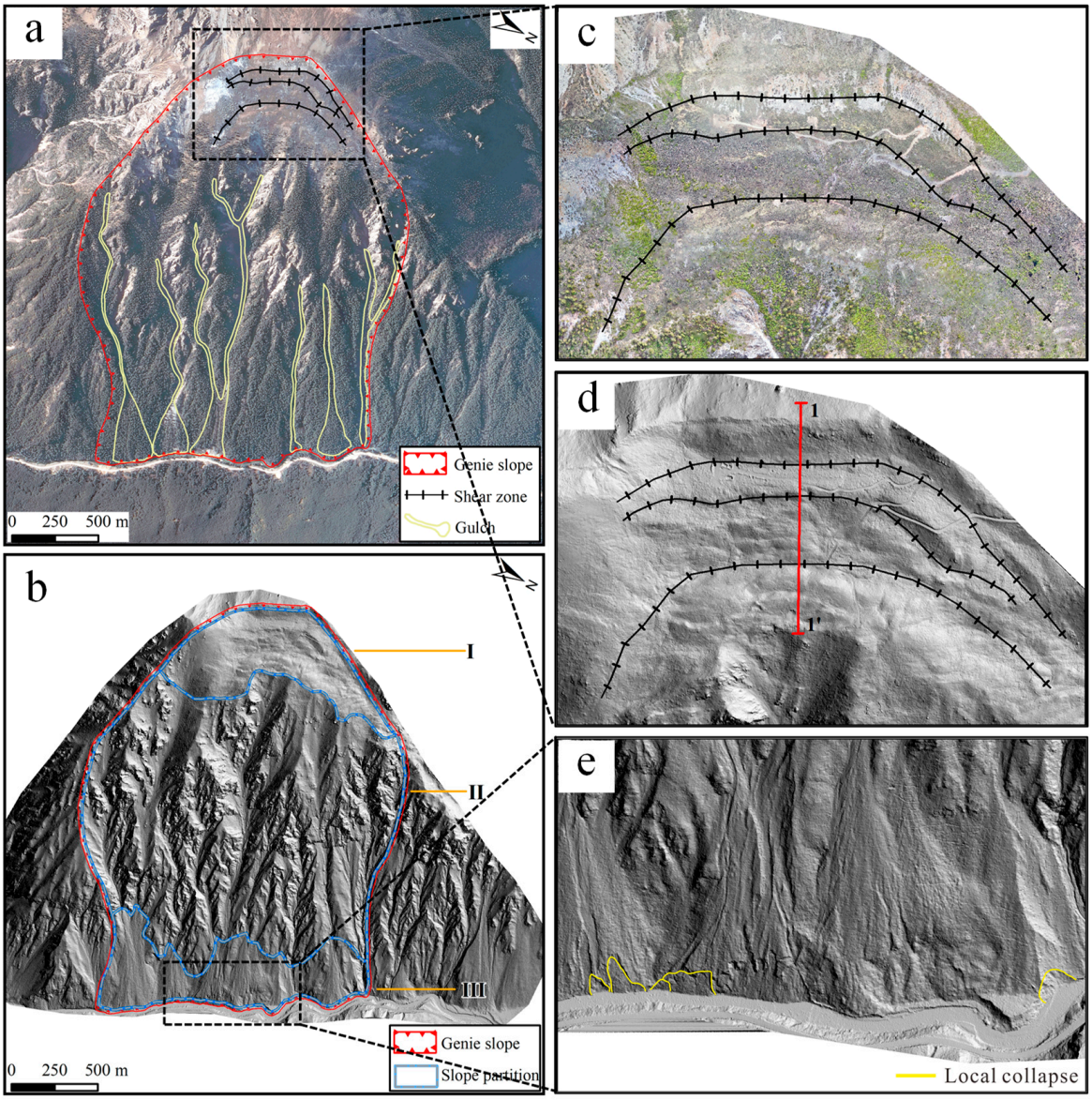



**Figure 4.** Interpretation results based on optical satellite images and airborne LiDAR data. (**a**) High-resolution optical satellite image interpretation; (**b**) LiDAR hillshade data interpretation; (**c**) large partial sample of an orthoimage at the trailing edge of the slope; (**d**) large partial sample of the hillshade data at the trailing edge of the slope; (**e**) large partial sample of the hillshade data at the front edge of the slope.

Zone I, located along the trailing edge of the slope, exhibits a crescent-shaped area of tensile cracking and dislocation. The rock mass in this zone is subjected to bending, tensile cracking, and intense weathering. It is heavily fractured due to well-developed joints and fissures, with the slope surface covered by Quaternary residual slope deposits. Additionally, three main dislocation zones divide the top area into three terraces (Figure 4c,d). A geological profile (1–1′) drawn using a DEM with vegetation removed reveals a maximum measured displacement height of approximately 40 m (Figure 5a,b).

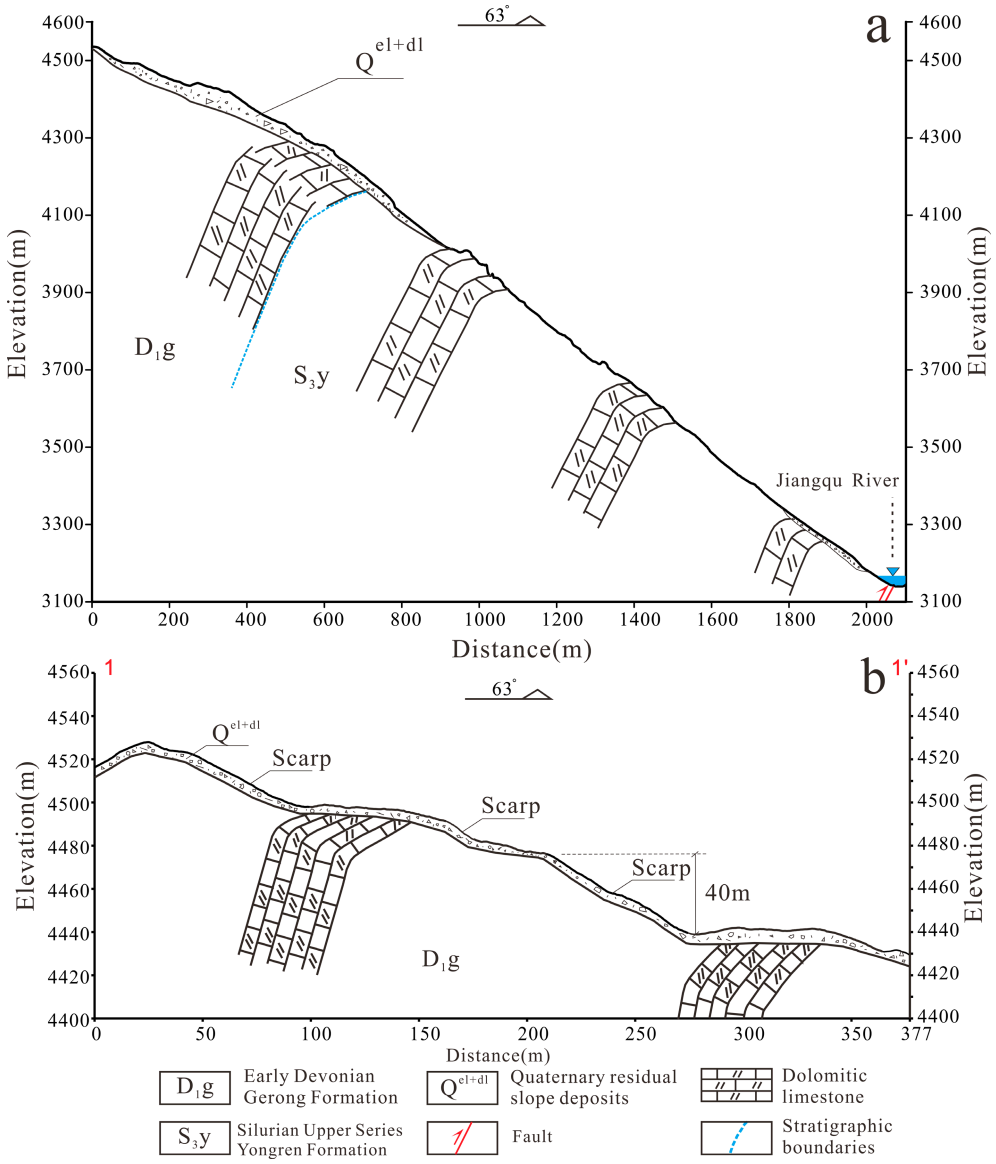



**Figure 5.** Geological profile of the Genie slope. (**a**) Overall profile of the slope; (**b**) 1–1′ geological section across the trailing edge of the slope.

Zone II, situated at the center of the slope, is characterized by significant deformation. The exposed bedrock in this area is highly fragmented, and small-scale collapses and rockfalls are common. Most rockfalls occur along seven major fully developed gullies.

Zone III, located at the foot of the slope, is influenced by erosion from the Jinsha River east boundary fault and scouring from the Jiangqu River. Collapses and slope surface debris flows are locally observed in this area. While many boulders and gravel soils accumulate at the mouth of the gully, the river channel remains unblocked (Figure 4e).

Three-dimensional analysis of the DEM and hillshade data after vegetation removal (Figure 6a) revealed outcrops of rock layers in the lower and middle areas on the right side of the mountain. Figure 6b illustrates the rock layers from the perspective of the slope's strike direction. Utilizing the fitting plane method, the attitude of the layer was measured to be 262°∠59°. In Zone II, two sets of structural planes, which form a set of conjugate planes, are predominantly exposed within the slope body (Figure 6c). The occurrence of these structural planes in a typical area (Figure 6c) was 164°∠48° for structural plane 1 and 318°∠41° for structural plane 2.

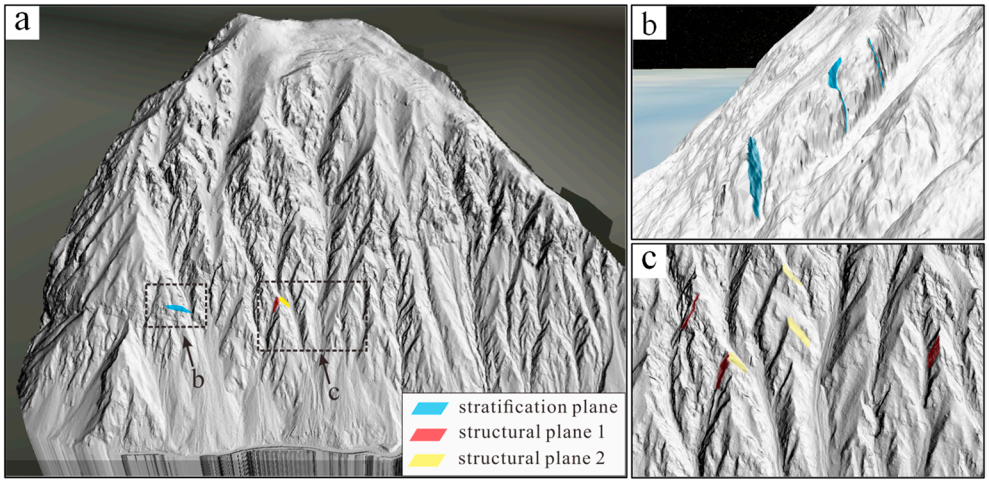



**Figure 6.** 3D model and structural surface identification of the Genie slope. (**a**) Visualization of the hillshade data; (**b**) occurrence of rock strata; (**c**) occurrence of structural planes.

### *4.2. InSAR Deformation Detection Results*

Four typical D-InSAR interferograms obtained from the ALOS-1 data were selected for display with the following dates: 31 January 2007 and 18 June 2007, 18 June 2007 and 3 August 2007, 3 August 2007 and 3 November 2007, and 20 September 2008 and 21 December 2008 (Figure 7). The differential interferogram of 31 January 2007 and 18 June 2007 has a lower quality due to the longer time interval, while the remaining three differential interferograms are of high quality. There is a small amount of residual noise phase in the four interferograms, but the remaining noise phase has a negligible influence on the overall result. The results show no clear or continuous periodic phase changes in the whole range of the slope, indicating that these interferograms of the slope contain no deformation.

The Sentinel-1A data were processed using Stacking-InSAR, with weighted averages calculated annually from 2017 onward. Weighted average interferometric stacking graphs were generated for four periods: March 2017 to December 2017, March 2017 to December 2018, March 2017 to December 2019, and March 2017 to November 2020 (Figure 8). During InSAR processing, the interferogram phases primarily encompass deformation, atmospheric errors, topographic errors, orbit errors, and noise. Achieving deformation resolution necessitates the separation of these phases, ultimately retaining only the deformation phase. Orbital error phases can be mitigated by employing precision orbital data from Sentinel-1, requiring the precision of the data to surpass 1 mm. Topographic phases can be addressed by simulating reference DEM data, with higher resolution DEM data resulting in cleaner removal of topographic error phases. Atmospheric errors are categorized into systematic and stochastic types; systematic atmospheric errors related to topography can be mitigated using reference DEM data, while stochastic atmospheric errors can be alleviated through high-pass filtering in the time domain. Noisy phases can typically be suppressed using filtering techniques. Following the removal of topographic effects and the application of flattening and filtering to eliminate noise and atmospheric effects, the four interferometric stacking diagrams depicted in Figure 8 exhibit smooth

phase transitions devoid of abrupt phase changes. This further substantiates that significant deformation is not evident in the slope.

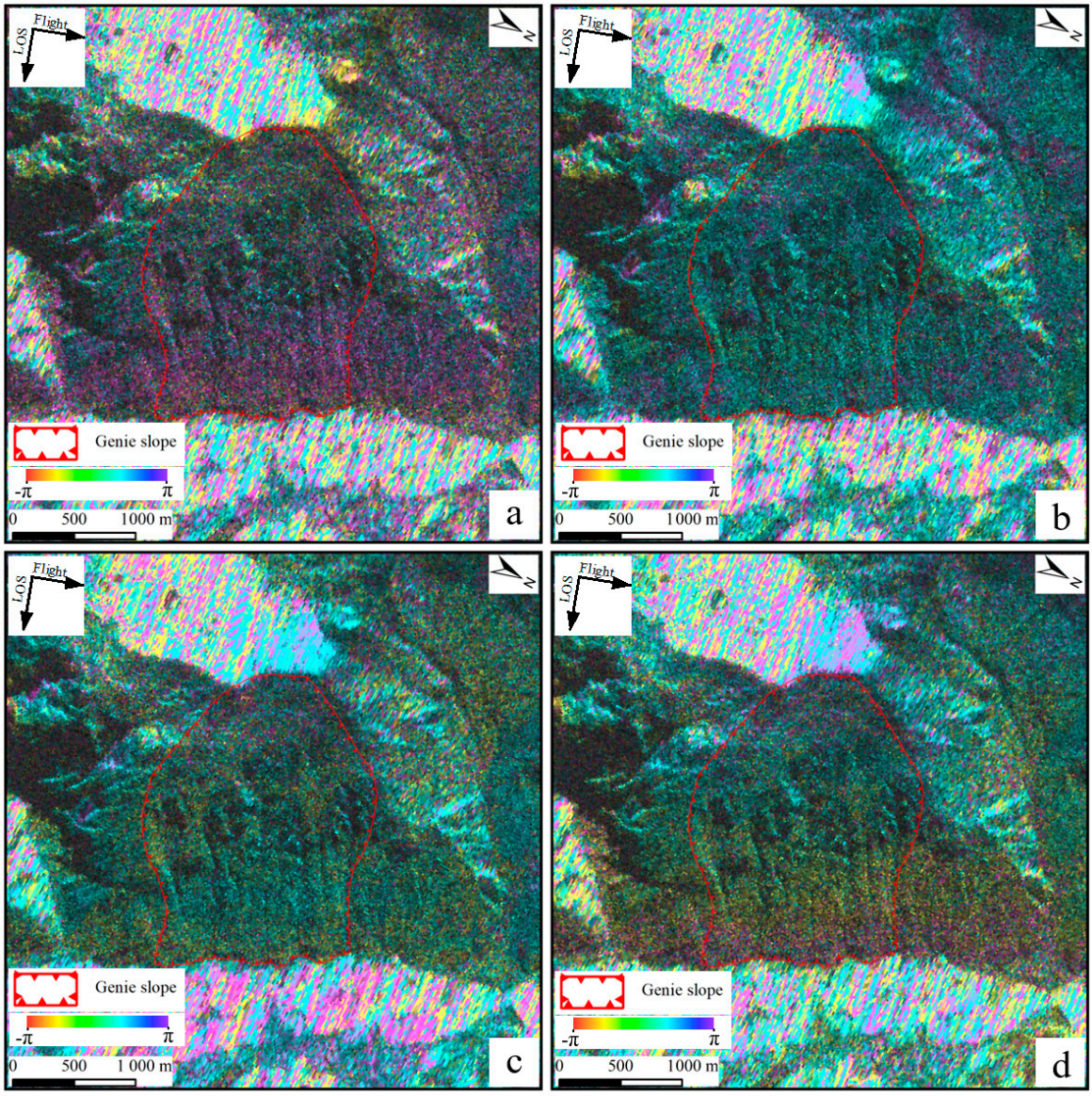



**Figure 7.** Typical differential interferograms of the Genie slope. (**a**) 31 January 2007 and 18 June 2007; (**b**) 18 June 2007 and 3 August 2007; (**c**) 3 August 2007 and 3 November 2007; (**d**) 20 September 2008 and 21 December 2008.

Additionally, the deformation of the slope was analyzed using SBAS-InSAR, and the average deformation rate of the slope was plotted (Figure 9). In this representation, a negative deformation rate indicates movement away from the satellite sensor, while a positive value indicates movement toward the sensor. The SBAS-InSAR results for the average deformation rate were combined with optical imagery, revealing that the vegetation coverage on the slope in Zone III exceeded that in Zones I and II. Consequently, coherence in Zone III is compromised, resulting in sparse data points for obtaining the deformation rate. Nevertheless, as depicted in Figure 9, the deformation rates at all points on the slope are predominantly concentrated near 0 mm/yr.

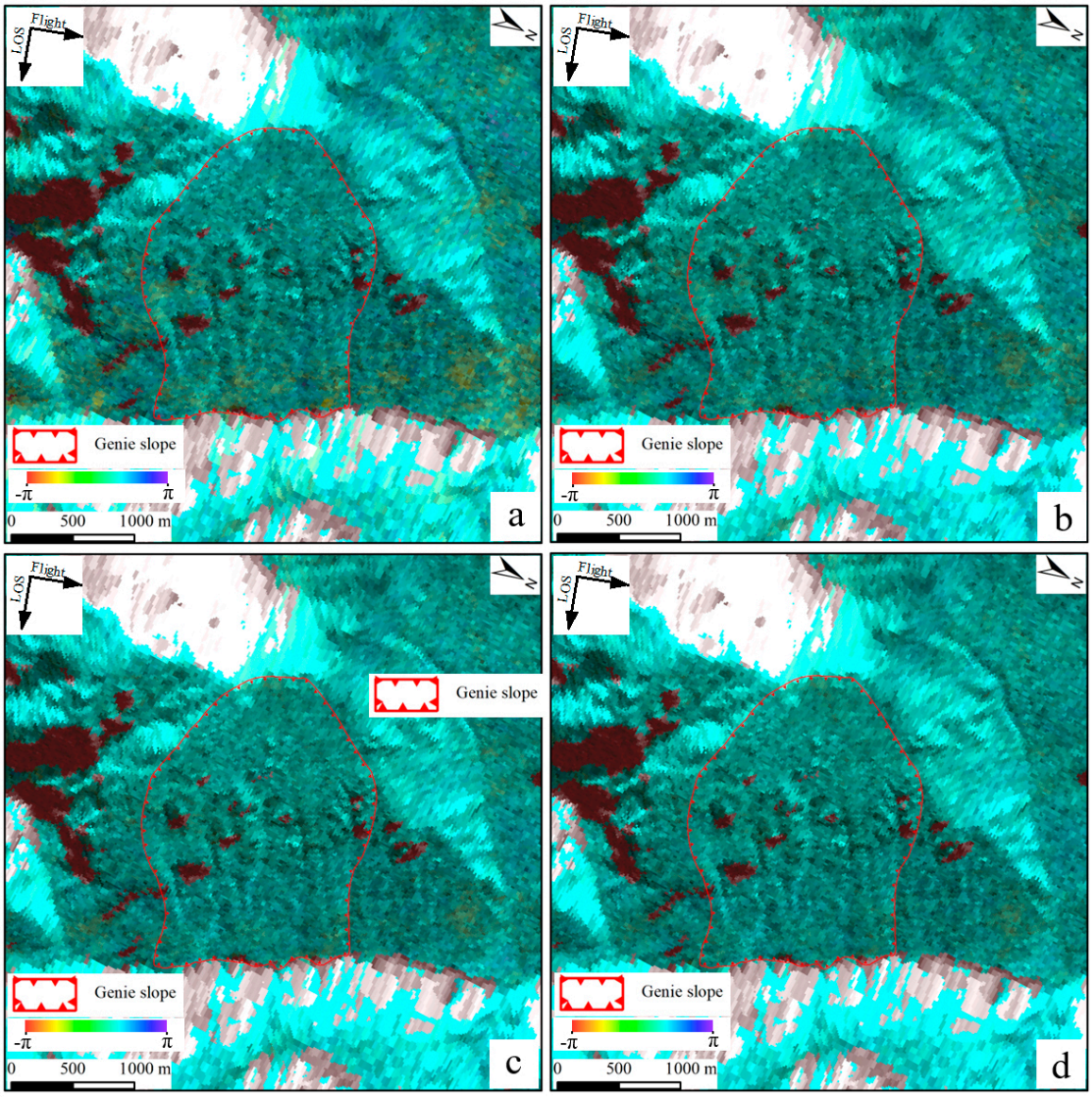



**Figure 8.** Stacking-InSAR interferometric stacking plots of the Genie slope. (**a**) March 2017 to December 2017; (**b**) March 2017 to December 2018; (**c**) March 2017 to December 2019; (**d**) March 2017 to December 2020.

To further analyze the deformation of the slope, an along-dip profile (profile 1–1′) was selected longitudinally along the slope surface, and an along-strike profile (profile 2–2′) was established in the middle of the slope (Figure 9); profile 1–1′ runs through all three zones, while profile 2–2′ runs transversely through Zone II. Five typical deformation points (A through E) were selected on profile 1–1′, while four typical deformation points (F through I) were selected on profile 2–2′. The average deformation rate of each profile is plotted in Figure 10, and the historical deformation curves at the typical deformation points between March 2017 and November 2020 are plotted in Figure 11. Table 2 shows the magnitudes of cumulative deformation, the average deformation rate, the area in which the deformation points are located, and the standard deviation of the phase residuals of the nine typical deformation points over a three-and-a-half-year period. Figure 10 demonstrates that while deformation rates at specific points on the profiles may appear anomalous, the majority of points on both profiles exhibit deformation rates within the range of −2 mm/yr to 6 mm/yr. Additionally, we fit the deformation rates using the reciprocal of standard deviation of the phase residuals at each point on the profiles as weights. The results indicate that despite

fluctuations in deformation, the overall deformation rate remains stable, characterized by very small orders of magnitude. In this study, reliability is assessed through the standard deviation of the phase residuals, which serves as a measure of errors arising from noise, topography, shadows, and deformation gradients during the phase unwrapping process. A lower standard deviation indicates a higher reliability of the InSAR results. The standard deviation of the phase residuals for each point ranged between 0.7 and 2.4 radians. Notably, the maximum phase residuals among the nine typical deformation points amounted to 2.2 radians. When converted to the centimeter scale, this equates to only 12.2 cm, which is deemed acceptable for the Genie slope covering an area of 3 $km^2$. Furthermore, Figure 11 illustrates that the magnitudes of cumulative deformation at the nine typical deformation points varied within a range of approximately $\pm$20 mm over the three-and-a-half-year period. To analyze these variations, we employed a nonlinear curve-fitting approach, using a third-order polynomial, for each of the two profiles. Remarkably, the overall trend of the cumulative deformation, as depicted by the fitted curves, closely resembles a straight line at the 0 mm scale. This observation supports the conclusion that the slope remained largely stable throughout the monitoring period. From the deformation analysis of profiles and typical points, it is evident that both the rate curves and deformation curves show localized jumps. We collected monthly rainfall data and observed that the overall trend of historical InSAR displacement does not strongly correlate with rainfall. This suggests that these fluctuations are not likely caused by rainfall-induced slope deformation. Instead, we attribute this occurrence to external factors such as topography, atmospheric conditions, and noise affecting the InSAR technique. Despite efforts to minimize these effects through processing, residual topographic and atmospheric errors can still contribute to localized fluctuations in deformation monitoring results. Throughout its history, InSAR technology has undergone continuous refinement aimed at reducing these errors and achieving a closer approximation to real surface deformation.

Early studies have indicated that surface deformation detected by InSAR, based on phase information, tends to be approximately linear and slow [43–45]. Hence, we consider that the local fluctuations observed in the data may not necessarily represent actual slope deformation, especially when the overall trend of deformation remains constant. In addition, we observed that the effective deformation points of SBAS-InSAR are sparse in the accumulation area at the foot of the slope (Zone III). This is primarily due to reduced coherence caused by steep topography and dense vegetation cover (Figure 9). In such cases, InSAR and optical imagery have limitations, whereas judgments based on LiDAR data are more accurate. LiDAR data indicate that this area primarily consists of residual slope deposits, with localized collapses formed by river erosion at the foot of the slope. The disturbance of these superficial deposits does not significantly impact the stability of the entire rocky slope. Conversely, in the upper and middle parts of the slope, the terrain appears more rugged in both optical and LiDAR data, with sparse vegetation cover. This results in good coherence for InSAR and a larger number of effective deformation points in the region. While optical and LiDAR data suggest that the upper slopes may appear vulnerable to damage visually, the InSAR results effectively correct this perception. In summary, the SBAS-InSAR results suggest that there is no significant deformation trend in the slope, leading to a preliminary assessment of its current state as being essentially stable.

Comparing the three InSAR techniques, D-InSAR yields the least favorable results. The primary reason is the long spatiotemporal baseline of the data used, which significantly affects coherence. Additionally, the limited capability for atmospheric error rejection in single-field differential interferograms impacts the outcomes. Stacking-InSAR addresses some of D-InSAR's limitations in atmospheric error rejection by employing extensive phase-weighted stacking, reducing the influence of random atmospheric errors that can be subsequently filtered out. In high mountain valley areas, atmospheric phase errors due to topography are estimated and corrected using an external reference DEM. However, this technique provides only the average deformation rate over the observation period and does not allow for historical deformation analysis. If slope deformation occurs briefly

before stabilizing, this short period may be mistaken for random atmospheric error and rejected during the weighted stacking process, resulting in erroneous outcomes.

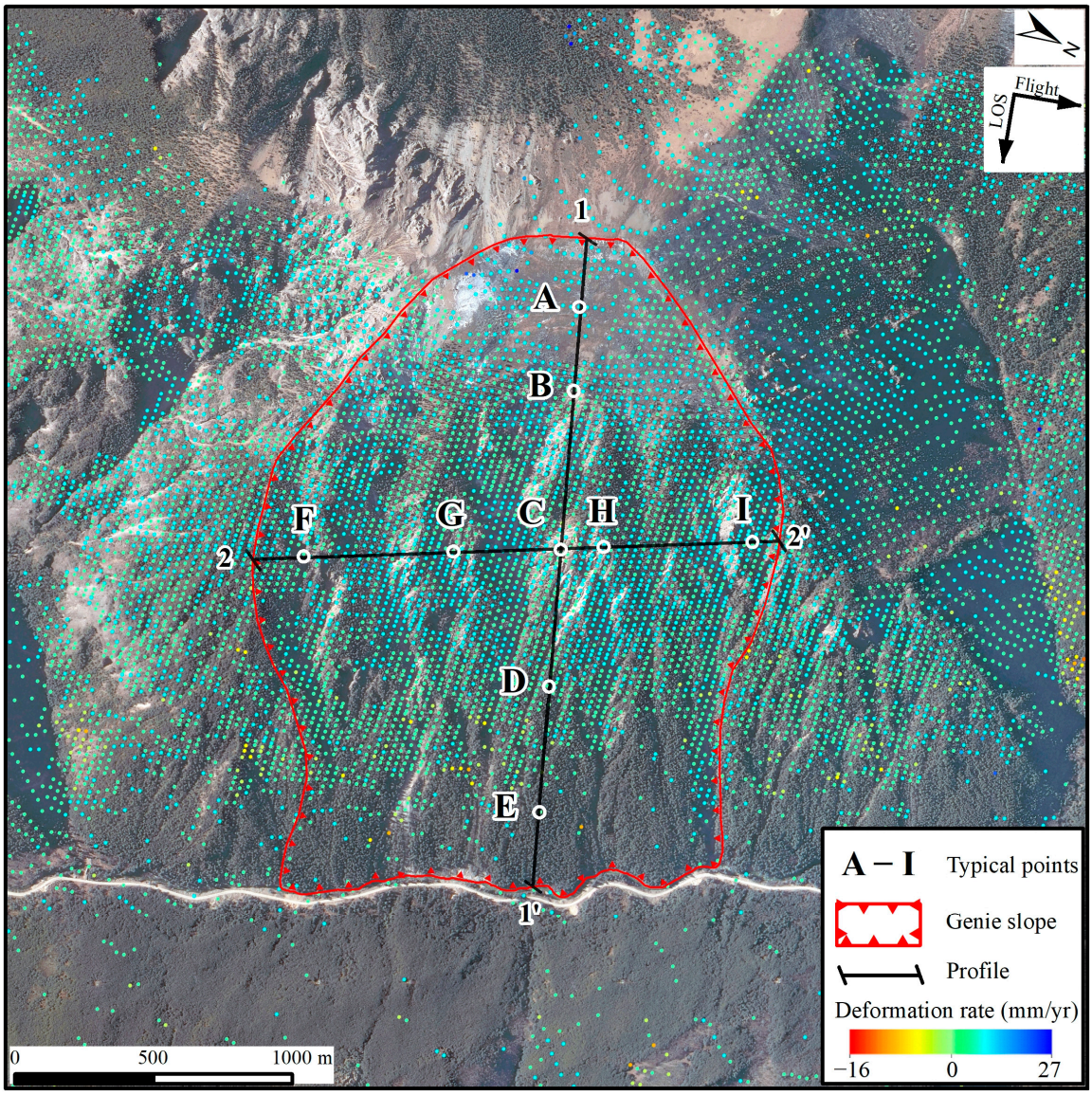



**Figure 9.** Average deformation rate of the Genie slope.

**Table 2.** Typical deformation point parameters.

| Parameters | 1–1′ Profile | | | | | 2–2′ Profile | | | |
|---|---|---|---|---|---|---|---|---|---|
| Point | A | B | C | D | E | F | G | H | I |
| Partition | I | II | II | II | III | II | II | II | II |
| Average annual deformation rate (mm/yr) | 0.2 | 1.0 | 3.7 | 4.7 | 1.1 | 4.4 | 2.6 | 3.6 | 1.4 |
| Cumulative deformation (mm) | 3.6 | −0.9 | 1.7 | 2.1 | 5.3 | −3.1 | −0.9 | 1.8 | 2.2 |
| Standard deviation of the residual phase (rad) | 0.9 | 1.0 | 0.8 | 0.8 | 2.2 | 0.9 | 0.7 | 1.1 | 0.7 |

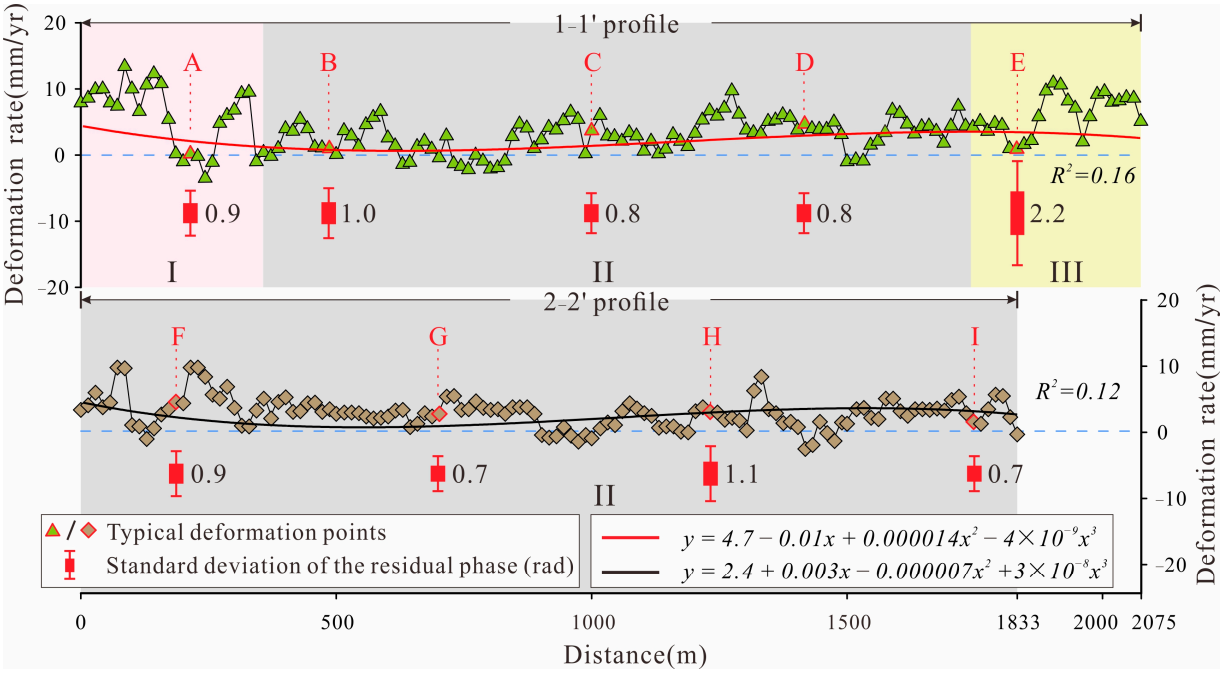



**Figure 10.** Average deformation rates along the 1–1′ and 2–2′ profiles. A weighted fit was conducted utilizing the phase residual standard deviation, with the error bars indicating the standard deviation of the phase residuals in the radian system at typical deformation points.

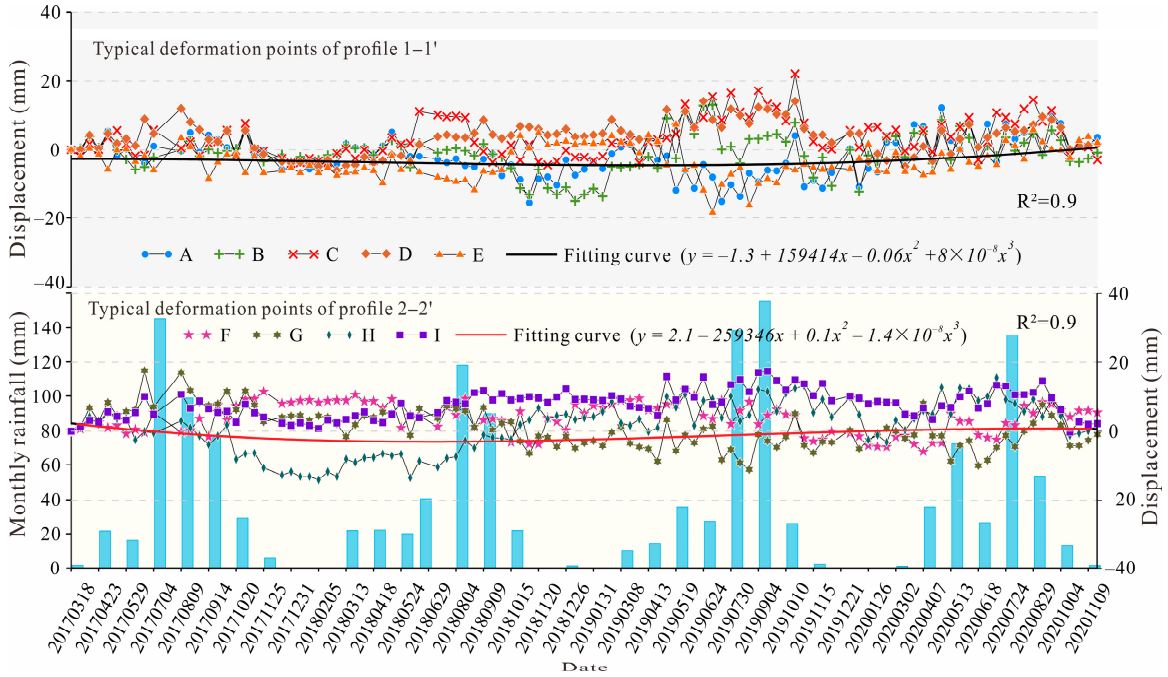



**Figure 11.** Cumulative displacements of typical points along the 1–1′ and 2–2′ profiles over the observation period. Points A–E are on the upper side of the 1–1′ profile, and points F–I are on the lower side of the 2–2′ profile.

SBAS-InSAR offers a more robust approach to capturing historical slope deformation, with higher reliability after applying coherence and standard deviation of phase residuals criteria. However, like other techniques, short-term deformations may yield minimal deformation rates in the solution, necessitating further evaluation through cumulative

variable curves. In conclusion, SBAS-InSAR represents the optimal choice for deformation analysis of single landslides in mountainous regions. D-InSAR and Stacking-InSAR can also contribute to the analysis under favorable weather conditions (minimal atmospheric phase influence) and with high-quality data (small spatial and temporal baselines).

### *4.3. Field Investigation and Exploration Results*

To validate the conclusions derived from integrated remote sensing, a series of field surveys were conducted, primarily comprising site reconnaissance, horizontal tunneling, and borehole monitoring. Field investigations revealed the presence of three distinct scarps along the rear edge of the slope, accompanied by trench-mounted sunken terrain at their bases (Figure 12a,c). In this area, the rocks display extensive fragmentation and high weathering, with gravel predominantly measuring 5–10 cm in diameter. The slope surface is largely covered with Quaternary residual slope deposits, supporting the growth of low shrubs and alpine meadows (Figure 12d,e). Toward the left rear edge of the slope, an early tension groove approximately 1.5 m in width is observed. The groove is filled with residual slope soil, and vegetation has taken root within. The rock formations flanking the tension groove exhibit severe fragmentation, rendering the layers and structural surfaces unrecognizable (Figure 12f). Bedrock is exposed in the middle of the slope, with the lower rock layer sharply inclined toward the slope's interior, while the upper rock layer bends outward (Figure 12b). Concurrently, isolated rock masses within the slope, detached from the matrix, undergo gradual weathering, forming unstable rocks. Although conspicuous scarps are evident along the rear edge of the slope, the vegetation in this area has largely recovered, with no discernible signs of fresh deformation. Upon analysis, it is inferred that these scarps likely resulted from the toppling failure of shallow rock layers during an earlier period, leading to the development of interlayer fractures.

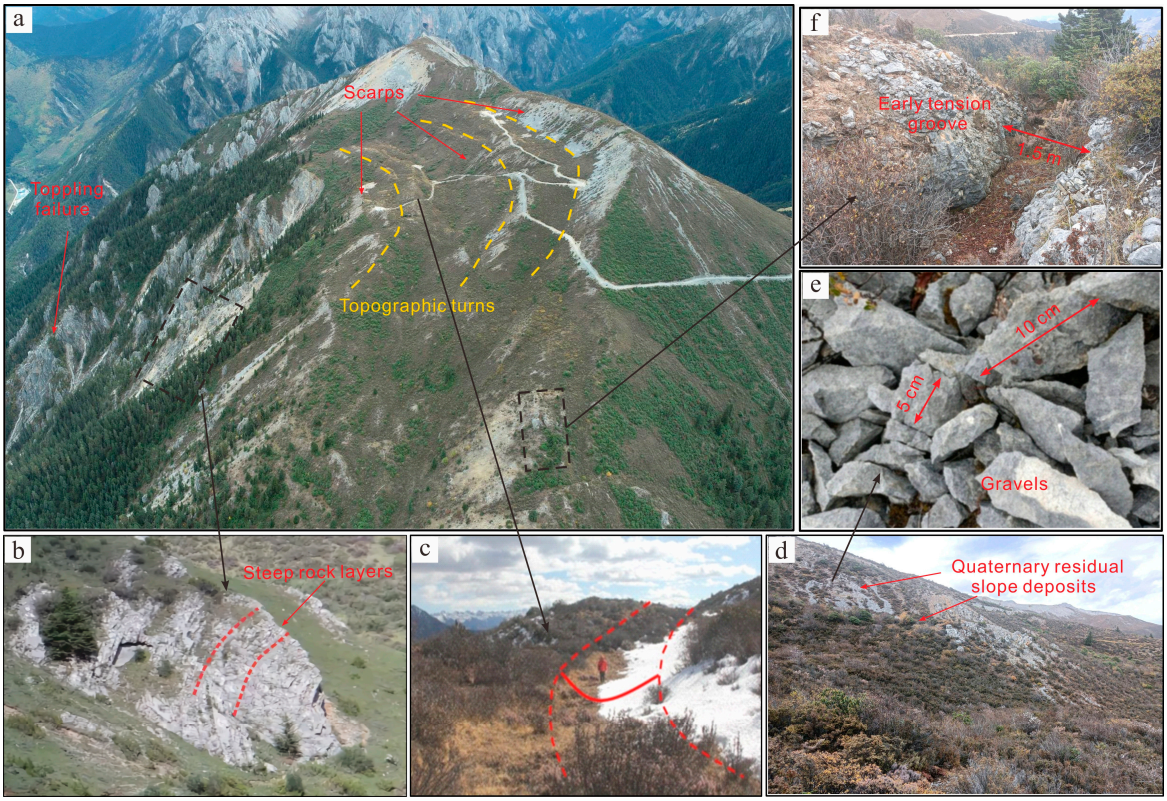



**Figure 12.** Field photos of the Genie slope. (**a**) Panoramic photo of the middle and rear of the slope; (**b**) morphological characteristics of the slope bedrock; (**c**) trench-mounted sunken terrain at the bottom of the scarp; (**d**) residual slope deposit overlay; (**e**) strongly weathered gravels; (**f**) rock mass tension groove.

This study collected data on the number, aperture size, and distribution of fissures and structural surfaces within a horizontal exploratory hole measuring 200 m in length and situated at an elevation of 3650 m above sea level on the slope. The rock quality improved gradually from the surface to deeper layers, with rock layers and interlayers inclined toward the inner side of the slope. Additionally, the primary joints of the rock body intersect the slope surface at a significant angle, consistent with the results obtained from LiDAR remote sensing interpretation.

Furthermore, the slope of the rock unit damage strain curve was analyzed to identify the depth of the unloading zone of the slope. As depicted in Figure 13, the extent of unloading in section AB exceeds that in section BC, tapering off after point C. Consequently, the region spanning 0–100 m (AB section) is identified as the strong unloading region, while the zone extending from 100 to 185 m (BC section) is characterized as the weak unloading region. Beyond point C lies the original rock stress region. This finding lends support to the conclusion that the scarps observed at the rear edge of the slope result from toppling failure of shallow rocks within an early strong unloading region.

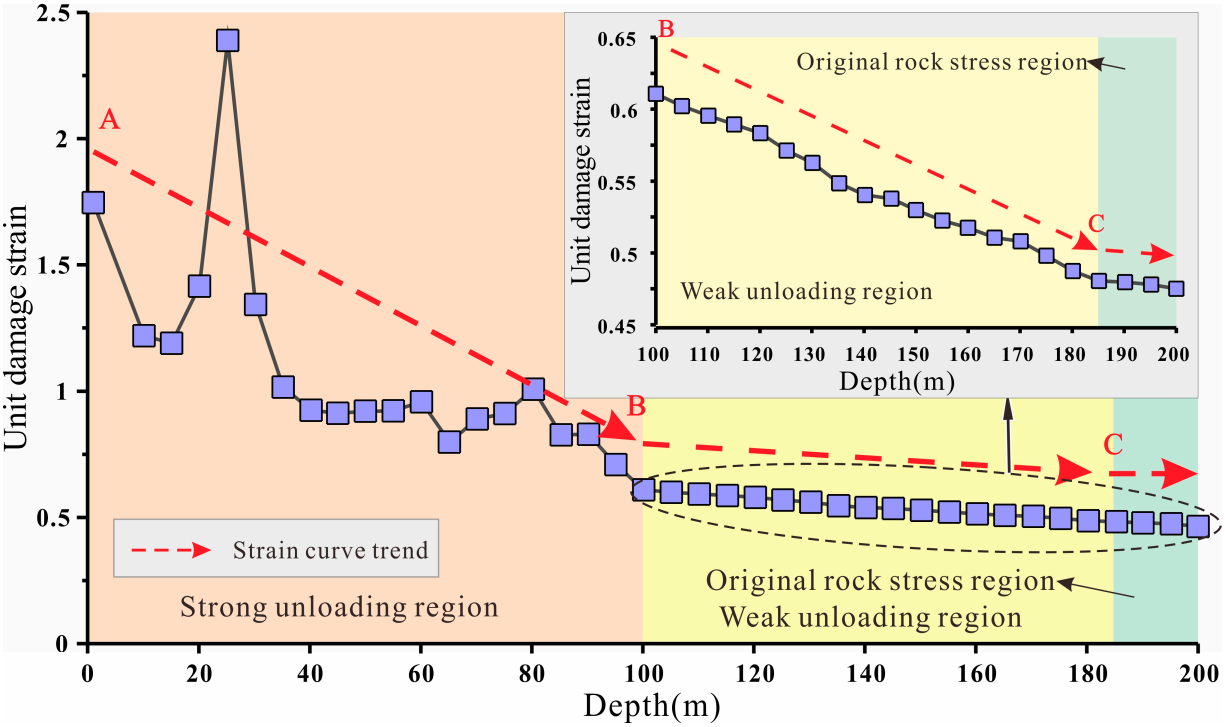



**Figure 13.** Unit damage strain curves and unloading zone delineation for the Genie slope.

To verify that there was no deformation in the InSAR results for the slope, displacement monitoring equipment was installed in borehole #2 at the top of the slope in 2021; the borehole displacement monitoring data showed very small horizontal displacement values of the slope, i.e., between −3 and 8 mm, which is consistent with the InSAR deformation monitoring results (Figure 14b).

In summary, the results of the investigation and analysis demonstrated that the slope has no obvious deformation at present, and this conclusion is consistent with the results of the comprehensive remote sensing analysis.

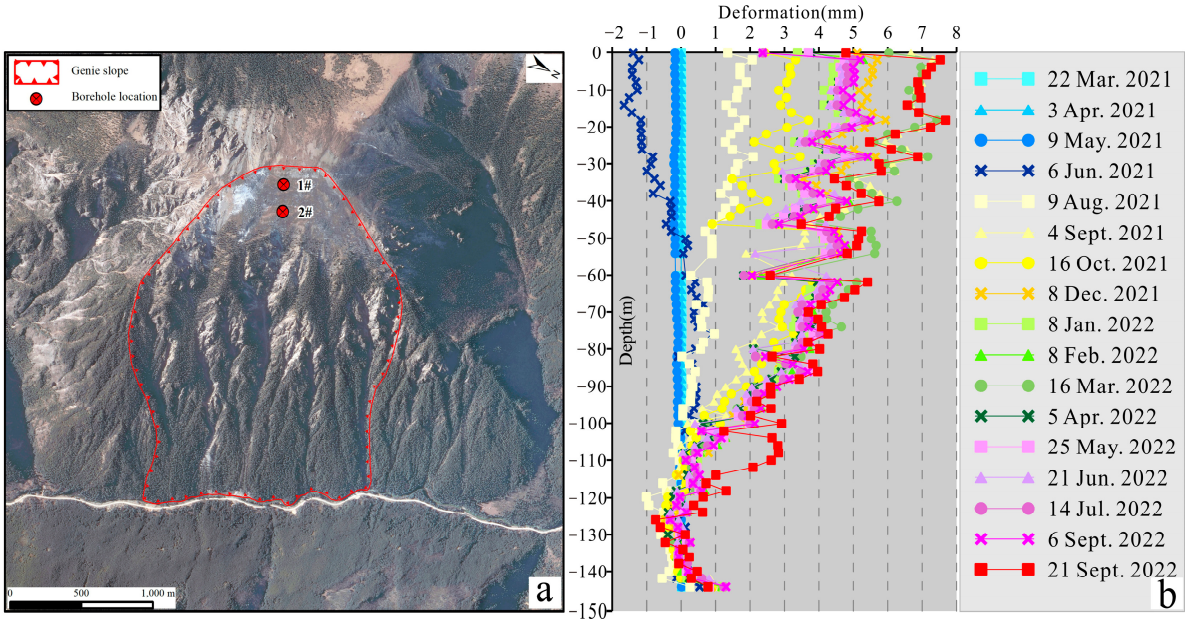



**Figure 14.** Borehole information for the Genie slope. (**a**) Borehole location and monitoring system; (**b**) horizontal displacements at different depths in the borehole.

## 5. Discussion

Individual remote sensing techniques have limitations in assessing geohazards and can sometimes even lead to incorrect conclusions. In contrast, integrated remote sensing exploits multiple remote sensing techniques by combining multiple sources of data, multiple indicators, multiple phenomena, and multiple results to conduct a comprehensive overall analysis of geohazards. The conclusions derived from this method are therefore more in line with reality. Finally, the current state of the slope can be identified by combining the results of field surveys and verification.

In this study, optical interpretation reveals distinct morphological features and indications of deformation on the Genie slope. The rear edge of the slope exhibits multiple stages of scarps, with fragmented rock surfaces showcasing numerous small-scale collapses and gullies. Airborne LiDAR data interpretation indicates that the rock mass in the middle of the slope is intersected by two sets of structural planes, resulting in a block-like structure overall. Furthermore, localized collapses of accumulated deposits are observed at the slope's corner. These geomorphological features suggest conditions conducive to slope failure.

However, despite these visual indicators, the D-InSAR monitoring results based on ALOS-1 data indicate no slope deformation between July 2007 and December 2008. Similarly, the time series InSAR monitoring results derived from Sentinel-1 data demonstrate no deformation between March 2017 and November 2020. Although InSAR deformation analysis is subject to various factors, such as external DEM accuracy, filtering strength, and atmospheric correction models, potentially leading to incomplete identification and rejection of extraneous phases related to terrain, noise, and atmosphere, the errors remain within acceptable limits, maintaining confidence in the final results. Consequently, the findings from these three InSAR methods collectively confirm the absence of deformation in the Genie slope.

Subsequent field survey results corroborate these findings, revealing no fresh signs of slope deformation. Instead, all the observed features are attributed to the early evolution of the slope.

Combining the available geological information and remote sensing data, the formation mechanism of the Genie slope is inferred to be as follows (Figure 15).

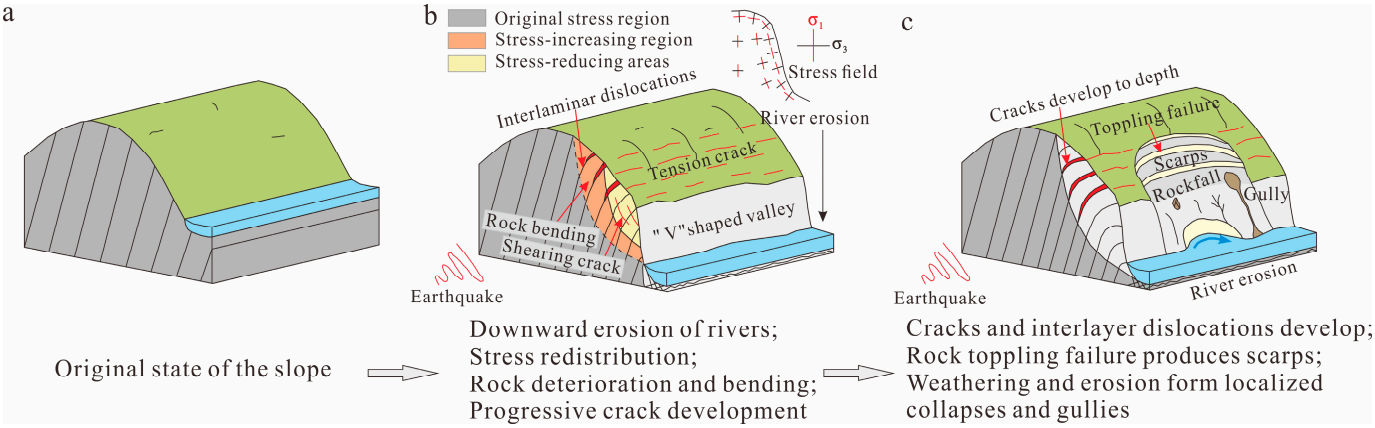



**Figure 15.** Schematic diagram of the slope deformation mechanism. (**a**) Original state of the slope; (**b**) cumulative damage state of the slope; (**c**) slope deformation and failure stages.

The Genie slope is situated in an area characterized by high geostress on the eastern edge of the Tibetan Plateau. Initially, the slope maintained equilibrium (Figure 15a). However, the process of river downcutting created a free surface, leading to the release of significant stresses within the slope. Consequently, unloading deformation occurred, resulting in stress redistribution.

As the river continued its rapid downcutting, the rock mass underwent degradation and plastic deformation due to the development of unloading cracks toward the slope's interior. This process further redistributed stresses within the slope, giving rise to distinct regions, such as stress-reducing, stress-increasing, and original rock stress regions, gradually extending from the slope surface toward its interior. The direction of stress was also adjusted, with the major principal stress aligning parallel to the slope surface and the least principal stress perpendicular to it. Tensile stresses were particularly prominent at the slope edge, leading to the folding and toppling of shallow, steeply inclined layers at the rear edge of the slope. This action, driven by tensile stresses and self-gravitational bending moments, resulted in interlayer dislocations and the formation of tensile cracks (Figure 15b).

Under natural conditions, the formation of scarps at the rear edge of the slope would have taken an extensive amount of time. However, the tectonic activity of the region, coupled with episodic earthquakes, significantly accelerated this process. The cyclic, opposing-direction tension and shear effects of earthquakes intensified the development of cracks and interlaminar dislocations to greater depths. Additionally, fractured rocks were ejected and deposited at the slope base, forming a first-stage scarp in situ. Once the first stage of scarp development reaches a certain height, another stage of scarp development follows the same pattern at the upper edge of the scarp due to stress concentration (Figure 16).

Presently, the exposure of bedrock in the middle of the slope is governed by rock stratification and two primary groups of conjugate structural planes. Prolonged weathering has led to continuous erosion of the bedrock on the slope surface, resulting in localized collapse and rockfall events. Multiple gullies have formed under the downslope movement of collapsing slope surface material and rockfalls, while the area of accumulated deposits at the foot of the slope has experienced localized collapse due to long-term erosion by the river (Figure 15c).

In previous integrated remote sensing studies of slopes, two main approaches were commonly employed. One approach involves using the deformation calculation function of InSAR in conjunction with visual interpretation based on optical and LiDAR data to pinpoint areas of surface deformation. This method facilitates the construction of a comprehensive landslide database, allowing researchers to identify and analyze surface deformation patterns effectively [16,40,46,47]. The other category of studies focuses on analyzing the rate of landslide deformation. This is accomplished by utilizing historical

deformation results from time series InSAR, along with pixel offset tracking results derived from optical and LiDAR data at various periods. By integrating these data sources, researchers can assess the deformation stage of landslides and implement landslide monitoring and warning systems [48–50]. These approaches collectively provide valuable insights into slope stability and facilitate proactive measures for landslide risk management. Conventional InSAR studies typically concentrate on areas experiencing deformation, analyzing deformation curves alongside other data like rainfall, reservoir storage, and temperature, to study phenomena such as rainfall-induced landslides, reservoir landslides, and freeze-thaw landslides. In contrast, this paper takes a different approach by utilizing deformation-free conditions observed in InSAR data to qualitatively assess the stability of slopes crucial to the proposed Critical Transport Corridor project. This method, though not entirely novel, underscores the importance of considering non-deformation data in slope stability analysis. By leveraging InSAR data indicating the absence of deformation, the study infers that the slope is presently in an essentially stable state. This application of InSAR provides valuable insights beyond the detection of deformation, contributing to more comprehensive risk assessments in infrastructure planning and management.

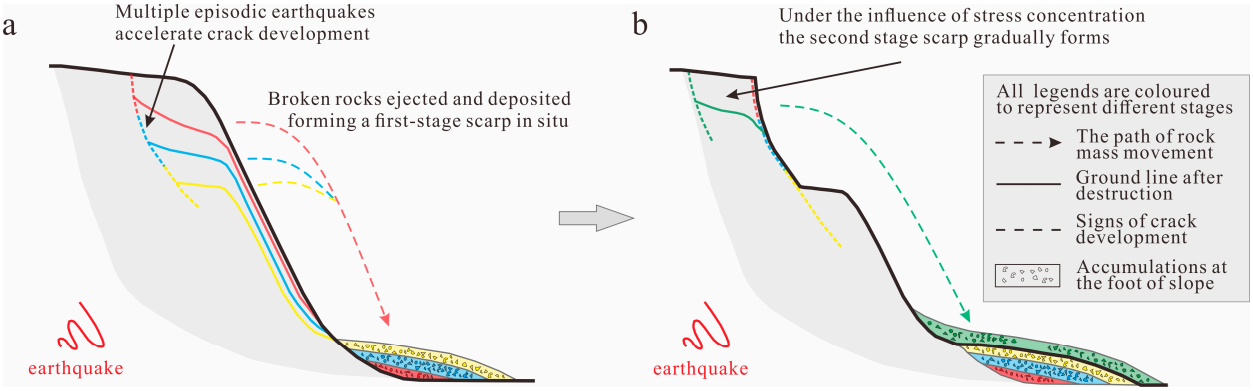



**Figure 16.** Schematic diagram of the multi-stage scarp mechanism. (**a**) Rapid development of cracks and interlayer misalignment due to episodic earthquakes, with damage leading to first-order scarps; (**b**) following the same pattern, earthquakes accelerate the development of second-order scarps on the base of preexisting terrain.

Optical imagery often reveals slopes along significant transport corridor projects that exhibit morphological characteristics and signs of deformation resembling those found in landslides. However, this does not necessarily imply that these slopes are at immediate risk of deformation and instability. Conducting detailed exploration of all such slopes using various techniques, such as boreholes, would incur excessive costs at the route proposal stage. Therefore, utilizing integrated remote sensing techniques for deformation analysis and preliminary stability assessment is an economically viable option.

Nevertheless, this approach still has limitations, with the accuracy and reliability of InSAR results being the most influential factors in stability assessment. In this study, the primary errors associated with the InSAR technique include atmospheric errors and phase unwrapping errors. As detailed in Section 4.2, terrain-related atmospheric errors and random atmospheric errors can be partially mitigated using external DEM data and filtering techniques. However, complete elimination of these errors is impractical; they can only be significantly reduced. This leads to anomalous jump points and fluctuations in InSAR deformation rates, which can mislead stability analysis. Phase unwrapping errors occur during the conversion of measured phases from $-\pi$ to $\pi$ into continuous phases. In surface deformation monitoring, these errors manifest in two ways: generating deformation signals that do not actually exist and altering the magnitude of actual deformation, both of which impact the final monitoring accuracy. These two main types of errors can create the illusion of deformation presence on stable slopes during assessment.

Previous wide-area InSAR deformation detection methods have focused primarily on identifying anomalous deformation locations on geosurfaces, allowing the interpretation of landslide boundaries via optical and LiDAR techniques. However, this approach does not impose stringent requirements on the deformation accuracy, potentially leading to erroneous judgments in areas with low coherence and high error rates. Therefore, it is essential to control these limitations by considering the standard deviation of the phase residuals to ensure the reliability of the obtained results. In addition to addressing the previously mentioned issues with InSAR technology, enhancing the feasibility of slope analysis in practical applications can be achieved by simultaneously analyzing SAR data with varying wavelengths, different observation angles, and shorter observation periods.

Notably, the study did not consider the disturbance of the slope structure by later tunnel excavation. Therefore, continuous analyses using integrated remote sensing, combined with InSAR and on-site instrumentation data, can still be used to monitor changes in slopes and to analyze their stability in detail during the tunnel construction period.

Based on this study, we propose an approach for investigating suspected landslides using integrated remote sensing technology during the construction of major transportation corridors. During the route selection phase, slopes exhibiting landslide characteristics are identified using optical remote sensing and airborne LiDAR. Subsequently, InSAR technology is employed to analyze historical deformations of these slopes and qualitatively assess their stability under natural conditions. Based on preliminary stability assessments, guidance is provided for route avoidance measures or specific management actions. During the construction phase, optical remote sensing and airborne LiDAR are utilized for surface visualization and analysis at various construction stages. InSAR is employed for real-time deformation monitoring, with data processing commencing from the project's initiation. This approach ensures that small deformations occurring during construction are not overshadowed by earlier natural state results lacking deformations, thus avoiding erroneous judgments. In the operational and maintenance phases of the corridor, InSAR serves as the primary monitoring tool, initiating monitoring from the corridor's official operational commencement. Optical and airborne LiDAR are intermittently used for less frequent corridor inspections, providing sufficient archived data for continuous monitoring and analysis.

## 6. Conclusions

Based on interpretations of optical remote sensing, airborne LiDAR, and InSAR deformation data, this paper investigates the slope of the Genie Tunnel on the Sichuan–Tibet transportation corridor. Through comprehensive analysis of the results obtained from these various remote sensing techniques, the surface deformation of the Genie slope is evaluated, and the slope formation mechanism is briefly assessed. The following four main conclusions can be drawn from this research:

1. Optical and LiDAR remote sensing data interpretation revealed that the Genie slope consists of steeply dipping inverted strata. Multistage scarps are observed in Zone I at the rear edge of the slope, while rock mass structural planes in Zone II in the middle of the slope contribute to local collapses. Additionally, accumulated deposits in Zone III at the foot of the slope are being eroded by the river. Consequently, the Genie slope exhibits morphological characteristics and deformation signs indicative of a potentially unstable slope based on optical and LiDAR visual interpretation.
2. The D-InSAR processing results for the ALOS-1 data and the Stacking-InSAR processing results for the Sentinel-1 data do not reveal significant deformation phases. Furthermore, the SBAS-InSAR processing results of the Sentinel-1 data indicate stable cumulative deformation of the Genie slope from March 2017 to November 2020, with mean deformation rates remaining at approximately 0 mm and 0 mm/yr, respectively, showing no significant trends. The credibility of this result is verified using the phase residual standard deviation, with the maximum standard deviation on the profile being 12.2 cm, which is deemed acceptable for the Genie slope with an area of 3 $km^2$.

In terms of deformation data, all three InSAR techniques used in this paper indicate that the Genie slope is presently not deformed and is in a stable state. To further confirm the accuracy of the InSAR results, a borehole displacement detection system was installed in 2021, revealing horizontal displacements consistently less than 8 mm from March 2021 to February 2022, indicating no slope deformation.

3. Based on survey data, a strong unloading region of the slope is identified between the slope surface and a horizontal distance of 185 m, where the rock exhibits significant deterioration and clear crack development. By integrating remote sensing and measured data, a conceptual model of the slope is developed, revealing that the multiple scarps observed in the optical image were formed by deformation of the rock layers in the strong unloading region of the Genie slope during an ancient evolutionary period. Conversely, the Genie slope currently shows no deformation under natural conditions.
4. The selection and design of railway routes in high-elevation mountainous and canyon regions often encounter situations similar to those of the Genie slope, where the individual interpretation of optical or LiDAR data over a slope may indicate a geohazard risk. However, the InSAR analysis results may suggest that the slope is not experiencing active deformation under natural conditions. Qualitative judgment of whether a slope exhibits deformation based solely on a single remote sensing technique becomes challenging in such cases. This research demonstrates that analyzing and determining slope deformation in alpine canyon areas from multiple factors, indicators, and perspectives using integrated remote sensing is not only feasible but also highly advantageous.

**Author Contributions:** Conceptualization, W.L. and W.Y.; methodology, W.Y.; software, W.Y.; validation, H.L.; formal analysis, W.Y.; investigation, D.W.; resources, Z.X., Z.W., P.L. and X.D.; data curation, W.Y.; writing—original draft preparation, W.Y.; writing—review and editing, W.L.; visualization, W.Y.; supervision, W.L.; project administration, W.L.; funding acquisition, W.L. All authors have read and agreed to the published version of the manuscript.

**Funding:** This research was funded by the National Key Research and Development Program of China (Grant No. 2021YFC3000401), the Key Research and Development Program of Sichuan Province (Grant No. 2023YFS0435), the State Key Laboratory of Geohazard Prevention and Geoenvironment Protection Independent Research Project (Grant No. SKLGP2022Z007), the Project of Ministry and Province Cooperation (Sichuan Geohazard 2023), and the Yangtze River Joint Research Phase II Program (Grant No. 2022-LHYJ-02-0201).

**Data Availability Statement:** The data that support the findings of this study are available from the corresponding author upon reasonable request.

**Acknowledgments:** We thank the ESA for the Sentinel-1 data.

**Conflicts of Interest:** Author Zhanglei Wu was employed by the company Chengdu Engineering Co., Ltd. Authors Zhengxuan Xu and Dong Wang were employed by the company China Railway Eryuan Engineering Group Co., Ltd. Author Pengfei Li was employed by the company Guiyang Engineering Corporation Limited of Power China. The remaining authors declare that the research was conducted in the absence of any commercial or financial relationships that could be construed as a potential conflict of interest.

## References

1. Peng, J.; Ma, R.; Lu, Q.; Li, X.; Shao, T. Geological hazards effects of uplift of Qinghai-Tibet plateau. *Adv. Earth Sci.* **2004**, *19*, 457–466.
2. Guo, C.; Zhang, Y.; Jiang, L.; Shi, J.; Meng, W.; Du, Y.; Ma, C. Discussion on the Environmental and Engineering Geological Problems along the Sichuan-Tibet Railway and Its Adjacent Area. *Geoscience* **2017**, *31*, 877–889.
3. Peng, J.; Cui, P.; Zhuang, J. Challenges to engineering geology of Sichuan-Tibet railway. *Chin. J. Rock Mech. Eng.* **2020**, *39*, 2377–2389. [CrossRef]
4. Xue, Y.; Kong, F.; Yang, W.; Qiu, D.; Su, M.; Fu, K.; Ma, X. Main unfavorable geological conditions and engineering geological problems along Sichuan-Tibet railway. *Chin. J. Rock Mech. Eng.* **2020**, *39*, 445–468. [CrossRef]

5. Cui, P.; Ge, Y.; Li, S.; Li, Z.; Xu, X.; Zhou, G.; Chen, H.; Wang, H.; Lei, Y.; Zhou, L.; et al. Scientific challenges in disaster risk reduction for the Sichuan-Tibet Railway. *Eng. Geol.* **2022**, *309*, 106837. [CrossRef]
6. Tian, S.; Wang, D.; Li, G.; Tao, W.; Shi, S. Design Concept and Main Principles of Tunnel on Sichuan-Tibet Railway. *Tunn. Constr.* **2021**, *41*, 519–530. [CrossRef]
7. Lu, C.; Cai, C. Challenges and Countermeasures for Construction Safety during the Sichuan-Tibet Railway Project. *Engineering* **2019**, *5*, 833–838. [CrossRef]
8. Zhao, B.; Su, L.; Wang, Y.; Li, W.; Wang, L. Insights into some large-scale landslides in southeastern margin of Qinghai-Tibet Plateau. *J. Rock Mech. Geotech. Eng.* **2023**, *15*, 1960–1985. [CrossRef]
9. Fan, X.; Xu, Q.; Alonso-Rodriguez, A.; Subramanian, S.; Li, W.; Zheng, G.; Dong, X.; Huang, R. Successive landsliding and damming of the Jinsha River in eastern Tibet, China: Prime investigation, early warning, and emergency response. *Landslides* **2019**, *16*, 1003–1020. [CrossRef]
10. Guo, C.; Yan, Y.; Zhang, Y.; Zhang, X.; Zheng, Y.; Li, X.; Yang, Z.; Wu, R. Study on the Creep-Sliding Mechanism of the Giant Xiongba Ancient Landslide Based on the SBAS-InSAR Method, Tibetan Plateau, China. *Remote Sens.* **2021**, *13*, 3365. [CrossRef]
11. Li, Y.; Chen, J.; Li, Z.; Han, X.; Zhai, S.; Li, Y.; Zhang, Y.; Gu, F. Comprehensive analysis of a paleo-landslide damming event on the upper reach of the Jinsha River, SE Tibetan Plateau. *Bull. Eng. Geol. Environ.* **2022**, *81*, 334. [CrossRef]
12. Liu, Y.; Yang, H.; Wang, S.; Xu, L.; Peng, J. Monitoring and Stability Analysis of the Deformation in the Woda Landslide Area in Tibet, China by the DS-InSAR Method. *Remote Sens.* **2022**, *14*, 532. [CrossRef]
13. Ouyang, C.; Zhao, W.; An, H.; Zhou, S.; Wang, D.; Xu, Q.; Li, W.; Peng, D. Early identification and dynamic processes of ridge-top rockslides: Implications from the Su Village landslide in Suichang County, Zhejiang Province, China. *Landslides* **2019**, *16*, 799–813. [CrossRef]
14. Guo, Z.; Chen, L.; Yin, K.; Shrestha, D.P.; Zhang, L. Quantitative risk assessment of slow-moving landslides from the viewpoint of decision-making: A case study of the Three Gorges Reservoir in China. *Eng. Geol.* **2020**, *273*, 105667. [CrossRef]
15. Zhao, C.; Lu, Z. Remote Sensing of Landslides A Review. *Remote Sens.* **2018**, *10*, 279. [CrossRef]
16. Lu, H.; Li, W.; Xu, Q.; Dong, X.; Dai, C.; Wang, D. Early Detection of Landslides in the Upstream and Downstream Areas of the Baige Landslide, the Jinsha River Based on Optical Remote Sensing and InSAR Technologies. *Geomat. Inf. Sci. Wuhan Univ.* **2019**, *44*, 1342–1354.
17. Hsu, C.; Tsao, T.; Huang, C.; Lee, C.; Lee, Y. Using Remote Sensing Techniques to Identify the Landslide Hazard Prone Sections along the South Link Railway in Taiwan. *Procedia Eng.* **2016**, *143*, 708–716. [CrossRef]
18. Su, F.; Guo, C.; Zhang, X.; Shen, W.; Liu, X.; Ren, S. Remote Sensing Interpretation of Large Landslides Along Sichuan-Tibet Railway Based on Object-oriented Classification Method. *Geoscience* **2017**, *31*, 930–942.
19. Glenn, N.; Streutker, D.; Chadwick, D.; Thackray, G.; Dorsch, S. Analysis of LiDAR-derived topographic information for characterizing and differentiating landslide morphology and activity. *Geomorphology* **2006**, *73*, 131–148. [CrossRef]
20. Jaboyedoff, M.; Oppikofer, T.; Abellan, A.; Derron, M.H.; Loye, A.; Metzger, R.; Pedrazzini, A. Use of LIDAR in landslide investigations: A review. *Nat. Hazards* **2012**, *61*, 5–28. [CrossRef]
21. Pellicani, R.; Argentiero, I.; Manzari, P.; Spilotro, G.; Marzo, C.; Ermini, R.; Apollonio, C. UAV and Airborne LiDAR Data for Interpreting Kinematic Evolution of Landslide Movements: The Case Study of the Montescaglioso Landslide (Southern Italy). *Geosciences* **2019**, *9*, 248. [CrossRef]
22. Miao, X. Application of multi-source remote sensing technology in the identification of debris flow source within complex mountainous areas in southeast Tibet. *Geol. Bull. China* **2021**, *40*, 2052–2060.
23. Tie, Y.; Xu, W.; Liang, J.; Meng, M.; Li, F.; Zhao, C. Characteristics of Kazila mountain landslide and its mitigation measures on the Sichuan-Tibet Railway. *Hydrogeol. Eng. Geol.* **2021**, *48*, 129–136. [CrossRef]
24. Pilecka, E.; Szwarkowski, D.; Stanisz, J.; Blockus, M. Analysis of a Landslide on a Railway Track Using Laser Scanning and FEM Numerical Modelling. *Appl. Sci.* **2022**, *12*, 7574. [CrossRef]
25. Kromer, R.; Hutchinson, D.; Lato, M.; Gauthier, D.; Edwards, T. Identifying rock slope failure precursors using LiDAR for transportation corridor hazard management. *Eng. Geol.* **2015**, *195*, 93–103. [CrossRef]
26. Hu, F.; Leijen, F.; Chang, L.; Wu, J.; Hanssen, R. Monitoring Deformation along Railway Systems Combining Multi-Temporal InSAR and LiDAR Data. *Remote Sens.* **2019**, *11*, 2298. [CrossRef]
27. Zhang, Q.; Li, Y.; Zhang, J.; Luo, Y. InSAR technique applied to the monitoring of the Qinghai-Tibet Railway. *Nat. Hazards Earth Syst. Sci.* **2019**, *19*, 2229–2240. [CrossRef]
28. Meng, X.; Qi, T.; Zhao, Y.; Dijkstra, T.; Shi, W.; Luo, Y.; Wu, Y.; Su, X.; Zhao, F.; Ma, J.; et al. Deformation of the Zhangjiazhuang high-speed railway tunnel: An analysis of causal mechanisms using geomorphological surveys and D-InSAR monitoring. *J. Mt. Sci.* **2021**, *18*, 1920–1936. [CrossRef]
29. Zhang, J.; Gao, B.; Liu, J.; Chen, L.; Huang, H.; Li, J. Early Landslide Detection in the Lancangjiang Region along the Sichuan-Tibet Railway Based on SBAS-InSAR Technology. *Geoscience* **2021**, *35*, 64–73. [CrossRef]
30. Zhang, J.; Zhu, W.; Cheng, Y.; Li, Z. Landslide Detection in the Linzhi-Ya'an Section along the Sichuan-Tibet Railway Based on InSAR and Hot Spot Analysis Methods. *Remote Sens.* **2021**, *13*, 3566. [CrossRef]
31. Dai, K.; Zhang, L.; Song, C.; Li, Z.; Zhuo, G.; Xu, Q. Quantitative Analysis of Sentinel-1 Imagery Geometric Distortion and Their Suitability along Sichuan-Tibet Railway. *Geomat. Inf. Sci. Wuhan Univ.* **2021**, *46*, 1450–1460. [CrossRef]

32. Bai, Y.; Xiong, X.; Tie, Y. Research on Early Identification of Landslide in Deeply Incised Valley of Sichuan-Tibet Railway. *J. Catastrophology* **2021**, *36*, 109–114. [CrossRef]
33. Gabriel, A.K.; Goldstein, R.M.; Zebker, H.A. Mapping small elevation changes over large areas: Differential radar interferometry. *J. Geophys. Res. Solid Earth* **1989**, *94*, 9183–9191. [CrossRef]
34. Williams, S.; Bock, Y.; Fang, P. Integrated satellite interferometry: Tropospheric noise, GPS estimates and implications for interferometric synthetic aperture radar products. *J. Geophys. Res. Solid Earth* **1998**, *103*, 27051–27067. [CrossRef]
35. Ferretti, A.; Prati, C.; Rocca, F. Nonlinear subsidence rate estimation using permanent scatterers in differential SAR interferometry. *IEEE Trans. Geosci. Remote Sens.* **2000**, *38*, 2202–2212. [CrossRef]
36. Rosen, P.; Hensley, S.; Joughin, I.; Li, F.; Madsen, S.; Rodriguez, E.; Goldstein, R. *Synthetic Aperture Radar Interferometry-Invited Paper*; IEEE: Piscataway, NJ, USA, 2000; Volume 88, pp. 333–382. [CrossRef]
37. Berardino, P.; Fornaro, G.; Lanari, R.; Sansosti, E. A new algorithm for surface deformation monitoring based on small baseline differential SAR interferograms. *IEEE Trans. Geosci. Remote Sens.* **2002**, *40*, 2375–2383. [CrossRef]
38. Crosetto, M.; Monserrat, O.; Cuevas-Gonzalez, M.; Devanthery, N.; Crippa, B. Persistent Scatterer Interferometry: A review. *ISPRS J. Photogramm. Remote Sens.* **2016**, *115*, 78–89. [CrossRef]
39. Dai, K.; Liu, G.; Li, Z.; Ma, D.; Wang, X.; Zhang, B.; Tang, J.; Li, G. Monitoring Highway Stability in Permafrost Regions with X-band Temporary Scatterers Stacking InSAR. *Sensors* **2018**, *18*, 1876. [CrossRef]
40. Xu, Q.; Zhao, B.; Dai, K.; Dong, X.; Li, W.; Zhu, X.; Yang, Y.; Xiao, X.; Wang, X.; Huang, J.; et al. Remote sensing for landslide investigations: A progress report from China. *Eng. Geol.* **2023**, *321*, 107156. [CrossRef]
41. Sandwell, D.; Price, E. Phase gradient approach to stacking interferograms. *J. Geophys. Res. Solid Earth* **1998**, *103*, 30183–30204. [CrossRef]
42. Strozzi, T.; Wegmuller, U.; Tosi, L.; Bitelli, G.; Spreckels, V. Land subsidence monitoring with differential SAR interferometry. *Photogramm. Eng. Remote Sens.* **2001**, *67*, 1261–1270. [CrossRef]
43. Jiang, M.; Li, Z.W.; Ding, X.L.; Zhu, J.J.; Feng, G.C.; Yin, H.J. A study on the maximum and minimum detectable deformation gradients resolved by InSAR. *Chin. J. Geophys.* **2009**, *52*, 1715–1724.
44. Li, M.; Zhang, L.; Shi, X.; Liao, M.; Yang, M. Monitoring active motion of the Guobu landslide near the Laxiwa Hydropower Station in China by time-series point-like targets offset tracking. *Remote Sens. Environ.* **2019**, *221*, 80–93. [CrossRef]
45. Liao, M.; Dong, J.; Li, M.; Ao, M.; Zhang, L.; Shi, X. Radar remote sensing for potential landslides detection and deformation monitoring. *Natl. Remote Sens. Bull.* **2021**, *25*, 332–341. [CrossRef]
46. Guo, C.; Xu, Q.; Dong, X.J.; Li, W.L.; Zhao, K.Y.; Lu, H.Y.; Ju, Y.Z. Geohazard Recognition and Inventory Mapping Using Airborne LiDAR Data in Complex Mountainous Areas. *J. Earth Sci.* **2021**, *32*, 1079–1091. [CrossRef]
47. Lu, H.; Li, W.; Xu, Q.; Yu, W.; Zhou, S.; Li, Z.; Zhan, W.; Li, W.; Xu, S.; Zhang, P.; et al. Active landslide detection using integrated remote sensing technologies for a wide region and multiple stages: A case study in southwestern China. *Sci. Total Environ.* **2024**, *931*, 172709. [CrossRef]
48. Xu, Q.; Zheng, G.; Li, W.; He, C.; Dong, X.; Guo, C.; Feng, W. Study on successive landslide damming events of Jinsha river in Baige village on October 11 and November 3, 2018. *J. Eng. Geol.* **2018**, *26*, 1534–1551.
49. Kang, Y.; Lu, Z.; Zhao, C.Y.; Zhang, Q.; Kim, J.W.; Niu, Y.F. Diagnosis of Xinmo (China) Landslide Based on Interferometric Synthetic Aperture Radar Observation and Modeling. *Remote Sens.* **2019**, *11*, 1846. [CrossRef]
50. Li, M.H.; Zhang, L.; Ding, C.; Li, W.L.; Luo, H.; Liao, M.S.; Xu, Q. Retrieval of historical surface displacements of the Baige landslide from time-series SAR observations for retrospective analysis of the collapse event. *Remote Sens. Environ.* **2020**, *240*, 111695. [CrossRef]


**Disclaimer/Publisher's Note:** The statements, opinions and data contained in all publications are solely those of the individual author(s) and contributor(s) and not of MDPI and/or the editor(s). MDPI and/or the editor(s) disclaim responsibility for any injury to people or property resulting from any ideas, methods, instructions or products referred to in the content.